International Journal of Fatigue 181 (2024) 108146

Contents lists available at ScienceDirect

International Journal of Fatigue

journal homepage: www.elsevier.com/locate/ijfatigue

Fatigue behavior of notched and unnotched AM Scalmalloy specimens subjected to different surface treatments

Santiago Aguado-Montero [a], Jesús Vázquez [a], Carlos Navarro [a,*], Jaime Domínguez [a,b]

[a] Department of Mechanical and Manufacturing Engineering, ETSI, Universidad de Sevilla, Spain
[b] ENGREEN, Laboratory of Engineering for Energy and Environmental Sustainability, Universidad de Sevilla, 41092 Seville, Spain

A B S T R A C T

In the present work, the fatigue resistance values of Scalmalloy specimens obtained by selective laser melting (SLM) additive manufacturing (AM) are experimentally studied. The fatigue levels of specimens with and without notches after applying different surface treatments, such as sand blasting, shot peening, isotropic finishing, and polishing alone or in combination, are analyzed. To understand the fatigue behavior of this material, the surface finishes and internal residual stresses of the specimens are analyzed. Moreover, the fracture surface of each sample is observed by electron microscopy to determine the failure mechanism. There is a clear separation between two different types of failure: (1) rupture by a crack generated on the surface associated with high applied stress values and (2) failure by a crack generated on an internal defect associated with low applied stress values.

1. Introduction

In some industrial sectors, such as the aerospace and automotive fields, reducing the weights of elements is very important for increasing efficiency because it leads to reductions in energy consumption and increases in payloads. Additive manufacturing, with the optimization of topologies and the use of lightweight alloys with high specific strengths, can reduce the weights of high-performance structural elements [1–4]. Titanium and aluminum alloys are the most common alloys for obtaining low-weight, high-strength structural elements [5–12]. There have been many studies about the AM of Ti alloy components, especially by SLM, and about methods for improving their mechanical properties [8–12]. However, Al alloys present more difficulties in being used for SLM production of structural pieces [5–7]. The low flowability, high reflectivity, high thermal conductivity and high susceptibility to oxidation of Al alloy powder necessitate a high laser power for SLM production resulting in increased porosities and residual stresses [13,14].

Among all Al alloys, cast Al-Si alloys are broadly used for SLM fabrication, especially AlSi10Mg and AlSi12 [5–7,15]. In addition, many analyses have been carried out to reduce porosity and improve mechanical properties through the optimization of manufacturing parameters [6,14,16] and through thermal and mechanical treatments after production [7,17–19]. For structural applications in aerospace and automotive applications, other hardenable alloys, such as the 2xxx, 6xxx and 7xxx series, are usually preferred. However, the wide range of solidification temperatures, high solidification shrinkage and thermal contraction of these alloys, and high energy density needed for processing by SLM cause these alloys to present some problems when processed by SLM, such as hot cracking [20–24], pores produced by the unstable processability of these alloys [25] and the partial evaporation of components [26]. A general view of the technology associated with Al alloy additive manufacturing can be seen in other research [13,17,22]. There has been much research to reduce these problems and obtain high-density pieces free from cracks. Some researchers have tried to eliminate hot cracking and reduce porosity by optimizing process parameters mainly in Al 7075 [21,23,27,28]; while hot cracking is reduced, it cannot be completely eliminated. Other scholars have proposed adding a small percentage of other elements to eliminate hot cracking and reduce porosity. Martin et al. [22] covered 7075 and 6061 powder with 1 vol% hydrogen-stabilized zirconium, changing the grain morphology during solidification, eliminating hot cracking and improving the mechanical properties of the SLM-produced material. Montero-Sistiaga et al. [20] added 4 wt% Si to 7075 powder to decrease the melting temperature and reduce the grain size during solidification, preventing the formation and propagation of cracks. Dadbakhsh et al. [26] added 6 wt% zinc oxide to 6061 powder to eliminate hot cracks; although this addition drastically reduces the number of cracks, they are not completely eliminated. Conversely, the addition of 2 wt% CaB_6 [24] or 0.7 wt% Ti [29] to 2024 powder eliminates the hot cracks in 2024 SLM-produced pieces. Despite all these efforts to eliminate hot cracks and improve the mechanical properties of these SLM-produced alloys, there are no analyses to date of

* Corresponding author.
E-mail address: cnp@us.es (C. Navarro).

https://doi.org/10.1016/j.ijfatigue.2024.108146
Received 29 September 2023; Received in revised form 14 December 2023; Accepted 1 January 2024
Available online 2 January 2024

their effects on improving the fatigue properties of these materials.

Special interest has been paid to the addition of Sc and Zr to Al-Mg alloys (5xxx series), which have been shown to produce high monotonic and fatigue strength, high ductility, and good creep and corrosion resistance [30,31]. On the one hand, increasing the Mg content produces strong solution strengthening [32]. On the other hand, nanoparticles of Al_3Sc act as grain refiners and precipitation hardening agents [31]. Additionally, the precipitation of nanoscale particles of Al_3(Sc, Zr) improves the strengths of AlMgScZr alloys through the stabilization of the grain structure during annealing treatments by inhibiting recrystallization softening [33,34]. These special characteristics, which have been studied for alloys used for pieces manufactured by traditional methods, have made the addition of Sc and/or Zr to Al alloys used for AM especially interesting.

Recently, some new alloys based on the addition of Sc and/or Zr to AlMg alloys [35–39] have been developed, especially for AM. A recently developed material is Scalmalloy®, developed by APWORKS GmbH [40]. This material is an aluminum alloy with high contents of Sc and Zr. This alloy offers an interesting synergy with additive manufacturing technologies since the rapid cooling that occurs in it allows the material to remain in a nonequilibrium state, preserving a significant amount of solute in solid solution. The Scalmalloy after AM presents a bimodal microstructure with zones of equiaxed fine grains combined with zones of coarse grains. The temperature regime and particle precipitation behavior characteristics are responsible for the duplex grain microstructure. During manufacturing, in the melt pool areas close to the melt pool, base particles of Al_3(Sc, Zr) and Al-Mg oxides act as nuclei for Al matrix solidification, resulting in a very fine-grained microstructure. In the hot melt pool areas (T > 800 °C), most particles dissolve, and coarse columnar grains grow [41]. The equiaxed fine grains, the bimodal microstructure and the precipitation of Al_3(Sc, Zr) make this low-anisotropy alloy very strong, ductile and susceptible to receiving a subsequent precipitation hardening treatment [41–45].

Concerning the fatigue strength and effects of different AM parameters and treatments on the fatigue behaviors of Al alloys, most analyses have been carried out with the ALSi10Mg alloy. There are many analyses about the effects of roughness [17,46,47], thermal treatment [17,19,48] and surface treatment, such as sand blasting, shot peening and laser shock peening [16,48–53].

In recent years, there have been several studies comparing the mechanical behaviors of Scalmalloys with other AM-based Al alloys [35,36,54] and analyzing the effects of AM parameters, roughness, heat and thermomechanical treatments on the microstructures and mechanical properties of Scalmalloys [41,43,44,55–60]. Moreover, there are few analyses on the fatigue crack growth behaviors of Scalmalloys [61–63]. However, there are other aspects of the fatigue behaviors of Scalmalloys that have either not been considered for analysis or not been analyzed deeply enough. For instance, the effects of shot peening and laser sock peening have received insufficient attention [56,64]. Additionally, to our knowledge, the effects of the stress gradient produced by the notches and fatigue behaviors of Scalmalloys with lives longer than 10^7 cycles have not been analyzed.

In the present work, we experimentally analyze the fatigue strengths of notched and plain Scalmalloy specimens obtained by selective laser melting (SLM)-based additive manufacturing (AM) with different surface finishes and treatments. The analysis is carried out for high- and very-high-cycle fatigue ($\leq 10^8$ cycles). The paper is organized as follows. First, the materials and methods used for the analysis are presented. Section 3 shows the results of monotonic tension testing, surface roughness and residual stress distribution produced by treatments. Afterward, the fatigue test results for notched and unnotched specimens are presented, and SEM images of the fracture surfaces are shown. A discussion of the results can be found in Section 4. Finally, some conclusions are obtained.

2. Methodology

2.1. Material

The specimens used in this study were manufactured by SLM additive manufacturing at AnyShape, and all of them received an aging heat treatment consisting of a temperature of 320 °C for 4 h. Table 1 shows the chemical composition of the powder and that measured in specimens manufactured. The values given for the powder are those specified by the producer. The manufacturing parameters were the commercial parameters used by the manufacturers of the specimens, with a 30-μm layer thickness. All specimens were manufactured in the z direction; that is, the layers were perpendicular to the test loading axis.

2.2. Geometry of specimens

Four different geometries, shown in Fig. 1, were used for the analyses performed. The first type of specimen, A, was used for tensile tests. The second type of specimen, B, with $d_{min} = 6$ mm, was used for plain fatigue tests. The third geometry, C, similar to the previous geometry, included a circular notch ($R = 1.5$ mm) so that the net section had a diameter of d = 6 mm. C was intended for notched fatigue tests. The stress concentration produced by the notch related to the net section was $k_t = 1.7$. Finally, a fourth geometry, D, indicated prismatic specimens with rectangular sections of 20x10 mm; it was used to perform measurements of roughness and residual stresses. To eliminate the small geometrical distortion produced during manufacturing and treatment, the ends of all A, B and C specimens were machined to guarantee a correct alignment of the loads and central zones of the specimens.

2.3. Surface treatments

All cylindrical specimens received a sand blasting treatment. Subsequently, the specimens of each type were distributed in groups, each of which received a different surface treatment, as explained below. Specimens type A and B were divided into five groups with the following treatments: sand blasting (SB) without additional treatment, polishing (POL), isotropic finishing (called superfinishing) (SF), shot peening (SP), and shot peening plus isotropic finishing (SPSF). Type C specimens were divided into three groups: SB, SP and SPSF. According to the AMS 2430 standard, the application parameter for the shot peeing treatment are: intensity 16–20 N, shots size AGB-35 (glass beads with hardness 500–550 HV) and a coverage of 200 %. Polishing treatment was applied manually on a lathe until a surface finish of $R_a = 0.06$ μm was achieved. The measurement of the diameter before and after polishing allowed us to determine that polishing eliminated a layer of 80 μm in thickness and 160 μm in diameter. Isotropic finishing is a kind of vibratory finishing combined with some chemical agent, designed by Curtiss–Wright®. Both treatments, SP and SPSF, were carried out by the company Curtiss–Wright. Finally, specimen type D, used for roughness and residual stress measurements, was divided into six groups: five groups with the same five treatments as the other type of specimens, SB, POL, SF, SP and SPSF, and another group including only the thermal treatment without sand blasting, which was called the as-built (AB) specimen group.

As a summary, Table 2 shows the surface treatments applied to the different specimens and the abbreviations herein used.

2.4. Tensile strength

The tensile tests were carried out in a 100-kN MTS servo-hydraulic testing machine. The tests were carried out with a displacement control and a speed of separation of the jaws of 0.5 mm/min. Three specimens were tested for each combination of surface treatments: SB, POL, SF, SP and SPSF.

Table 1
Chemical compositions of the Scalmalloy powders [26] and specimens manufactured.

	Element	Al	Mg	Sc	Zr	Mn	Si	Fe	Zn	Cu	Ti	O	V
Powder	wt.% (min)	Bal.	4.00	0.60	0.20	0.30	0.00	0.00	0.00	0.00	0.00	0.00	0.00
	(max)		4.90	0.80	0.50	0.80	0.40	0.40	0.25	0.10	0.15	0.05	0.05
Specimens	wt.%	Bal.	3.81	0.61	0.28	0.47	0.12	0.15	0.01	0.00	0.00	0.00	0.00

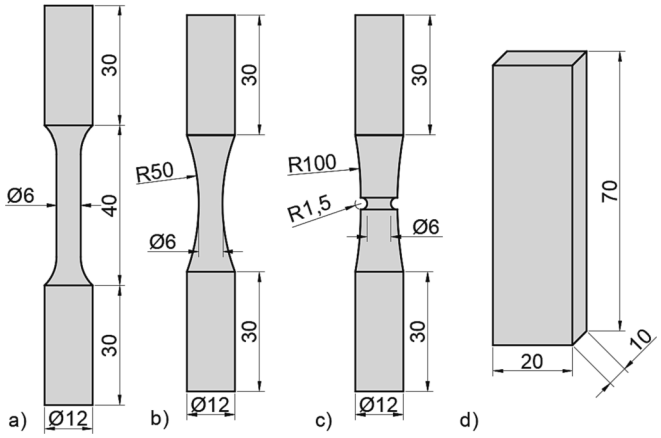

Fig. 1. Different types of specimens designed for the tests.

Table 2
Resume for the abbreviation and applied surface treatments.

Surface treatment	Abbreviation	Applies to specimen type
No treatment	AB	D
Sand Blasting	SB	A, B, C and D
Polishing	POL	A, B and D
Isotropic finishing	SF	A, B and D
Shot peening	SP	A, B, C and D
Shot peening + isotropic finishing	SPSF	A, B, C and D

2.5. Surface finish

The surface finish was characterized by a Mitutoyo Surftest 500/501 roughness tester. Ten measurements were taken for each surface treatment using the prismatic geometry specimens described in a previous section. Moreover, a laser confocal microscope SENSOFAR S NEOX and a scanning electron microscope FEI TENEO were used to analyze the surface topography.

2.6. Residual stresses

The residual stresses near the surfaces of specimens with different treatments were estimated on the prismatic geometry specimens using the blind hole technique (Sint MTS3000) and the integral method [65]. Four measurements were taken for each combination of treatments.

2.7. Fatigue tests

The fatigue tests were carried out in a 100-kN RUMUL Testronic resonance machine at a frequency of approximately 110 Hz and with zero mean stress (R = -1). Tests that reached a lifetime of 10^8 cycles were considered run-out tests. Twelve unnotched specimens were tested for each combination of treatments—SB, POL, SF, SP and SPSF—while only eight notched specimens were tested for treatment combinations SB, SP and SPSF.

2.8. Study of fracture surfaces

Fracture surfaces were analyzed using FEI TENEO SEM, and images of all fatigue fracture surfaces were taken. The main objective of SEM analysis was to determine the crack initiation, fatigue crack growth mechanisms and the position, size, and type of the critical defect where the crack initiated.

3. Results

3.1. Tensile strength

Fig. 2a shows the results of the tensile tests for specimens of the five groups of treatments. The figure includes the most important properties that are deduced from these tests. The figure shows that there are no significant differences between the groups of specimens. Fig. 2b shows the result of one of the tests carried out on an SP specimen.

3.2. Surface finish

Fig. 3 shows the roughness measurements (R_z and R_a) for different surface treatments. Each box represents the average of ten measurements plus/minus the standard deviation. As seen in the figure, the surface roughness is very high in specimens that have not received any surface treatment (AB). This finishing improves slightly when applying sand blasting (SB). The shot peening treatment (SP) does not seem to have a significant effect on the surface roughness produced by the previous sand blasting. Additionally, isotropic finishing treatments or superfinishing (SF) improve the roughness produced by sand blasting and shot peening. The average values and the standard deviation for the polished specimens (POL) are one order of magnitude smaller than the best value of the other treatments. Fig. 4 shows confocal microscopy images of the surfaces obtained with the treatments. The figure shows how the superfinishing mainly reduces the high-frequency irregularity but does not substantially affect the low-frequency irregularity. Fig. 5 shows the SEM images of the surfaces obtained with different treatments. The as-built surface shows powder particles adhered to the surface, while sand blasting and shot peening have eliminated those particles and made the surface increasingly uniform with similar characteristics for both treatments, although craters produced by shot peening are larger than those produced by sand blasting. Finally, the effects of superfinishing are similar for the sandblasted and shot peened surfaces.

3.3. Residual stresses

Residual stress measurements for each treatment combination are shown in Fig. 6. Solid lines represent the average values of the four measurements carried out for each treatment combination. Dashed lines represent the range of the measurements obtained. The specimens that have received exclusively the heat treatment, denoted by AB (as built), do not present significant residual stresses. It is interesting to note that although the objective of sand blasting (SB) is to clean the surface by eliminating adhered particles, it produces a thin surface layer with compressive residual stresses. The depth of the layer is approximately 150 μm, while the maximum residual compressive stresses produced are approximately 100 MPa. This residual stress field is not modified substantially by the subsequent application of the isotropic finishing or

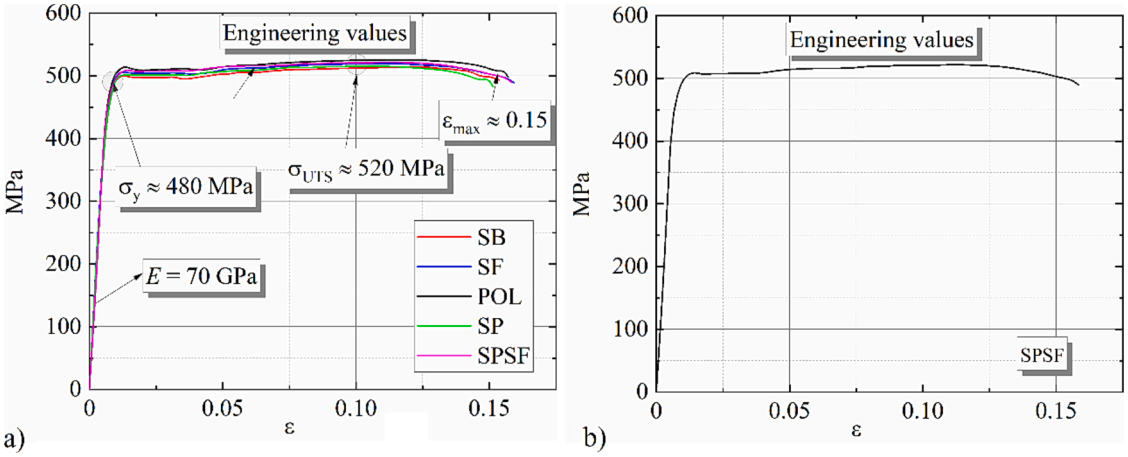

Fig. 2. Tensile test results. (a) Tests for specimens of the five groups of treatments and (b) results of one of the tests carried out for an SPSF specimen.

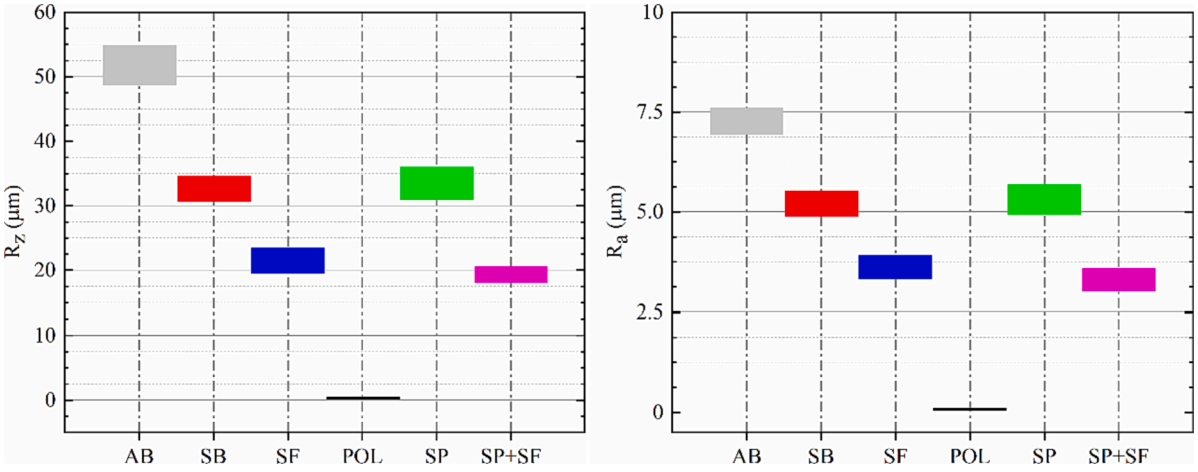

Fig. 3. Roughness measurements R_z and R_a.

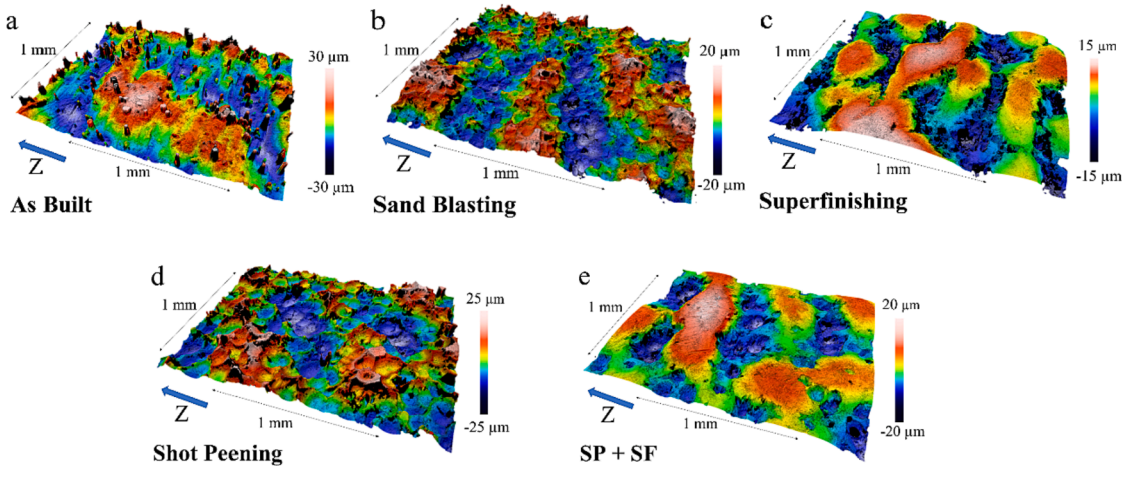

Fig. 4. Confocal microscope images of the treated surfaces.

superfinishing (SF) treatments. Notably, the specimens that received the sand blasting treatment followed by polishing (POL) contain hardly any residual stresses; thus, it is determined that this last treatment removes most of the layer of material affected by the previous treatment. Finally, the maximum residual compression stress values appear after the treatment of shot peening (SP), taking values reaching 250 MPa. The depth of the residual stress field produced is close to 300 μm. Appreciably, applying a subsequent treatment of isotropic finish or superfinishing (SPSF) has no effect on the residual stresses, which have values almost identical to those obtained after shot peening.

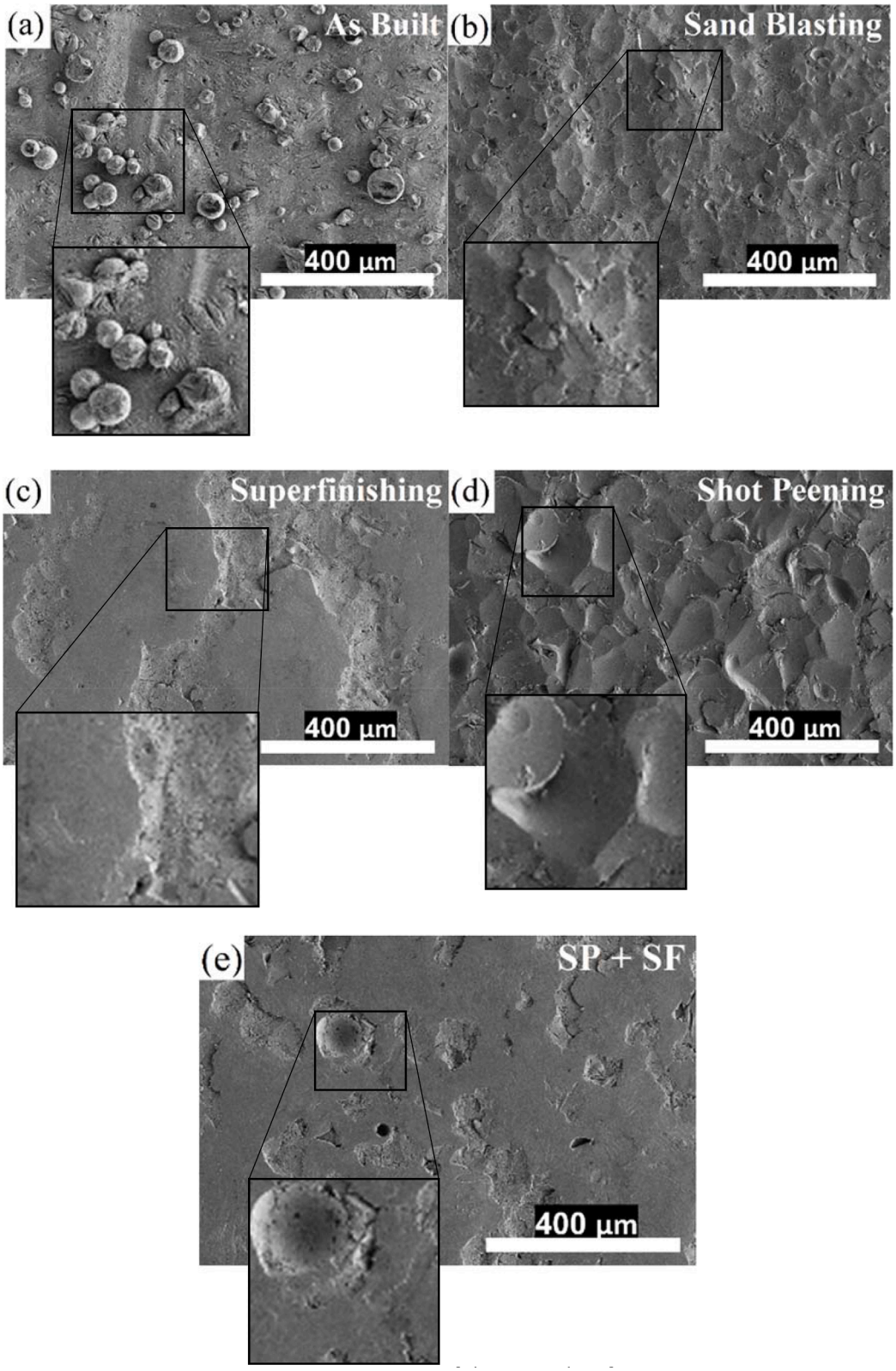

Fig. 5. SEM images of the treated surfaces.

3.4. Fatigue tests

The results of the fatigue tests are shown in Fig. 7. Fig. 7a contains the S-N curves of the smooth specimens, while Fig. 7b shows those curves for the notched specimens. Dots are experimental results, and the lines show the S-N curves fitted to the experimental results. Solid symbols represent failures produced from cracks initiated on the surface, and hollow symbols represent failures initiated from an internal defect in the specimen. Triangular symbols represent failures due to internal defects very close to the surface, which have only been found in polished specimens.

In all specimen groups, except for the unnotched samples that

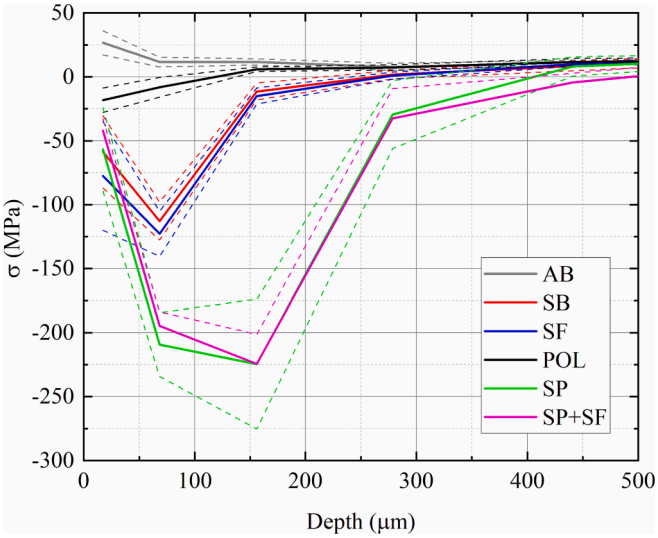

Fig. 6. Residual stresses measured.

received the shot peening treatment (SP and SPSF), the S-N curves have two zones with markedly differentiated slopes. The stress level at which the transition from one slope to another occurred is different for each specimen group; therefore, it depends on both the applied surface treatment and the specimen geometry.

In the case of the unnotched specimens (Fig. 7a), those that did not receive shot peening (SB, SF and POL) show no significant differences in the first zone of their respective S-N curves (high values of applied load and lives under $2x10^5$ cycles). However, we appreciate some divergences between their respective S-N curves for high lives, corresponding to relatively low applied loads. In this situation, the isotropic finishing treatment managed to slightly improve the fatigue strengths of the samples. Surprisingly, specimens that received the polishing treatment perform more poorly than those that do not, even though they have substantially better surface finishes.

In the unnotched specimens that received shot peening (SP and SPSF), we did not observe a clear change in the slope of the S-N curve. In addition, the fatigue curves for these two treatments are almost indistinguishable from each other. Thus, the isotropic finishing and superfinishing treatments do not seem to have any effect on the samples that previously received shot peening. In the tests in which the applied load is greater than approximately 200 MPa, the shot peening treatment significantly improves the fatigue resistance. However, as we approach the very high cycle fatigue regime, the results of all specimen groups seem to converge to similar values; thus, polishing, isotropic finishing and shot peening treatments have very little effect in this situation.

In the case of the notched specimens (Fig. 7b), all the treatments present an S–N curve with two sections with very different slopes. We observed that shot peening increases fatigue life in all cases, although its effect is more significant for lives under 10^6 cycles. For lives close to 10^8 cycles, the effect of shot peening is much smaller than that at 10^6 cycles. Again, we observed that the isotropic finishing treatment after shot peening has no appreciable effect on the fatigue resistance of the samples.

3.5. Analysis of fracture surfaces

The SEM analysis of all fracture surfaces resulting from fatigue tests provides important information about the type of failure of the groups of specimens subjected to different combinations of surface treatments. Three different fault typologies were detected.

The first failure type is the initiation of a crack from an internal defect. Fig. 8 shows two examples of this failure mode. In one case, the defect lacks fusion (Fig. 8a), while in the other (Fig. 8b), the defect is a pore. These types of failures are associated with tests of unpolished specimens in which the applied load is low. The load level below which this failure mode occurs depends on the treatment received by the samples. Fig. 7 shows by means of hollow symbols all the specimens that suffer this type of failure.

The second type of failure consists of the initiation of one or more cracks from the surface of the specimen, as shown in Fig. 9. This mechanism is associated with unpolished specimens subjected to high stress levels, usually producing lives under 10^6 cycles. These high loads frequently produce multiple initiation sites, as shown in the figure.

The third type of failure detected is associated with polished specimens. In these samples, the removal of a layer of approximately 80 μm of material causes internal defects present in the material at a certain depth from the surface to appear very close to the surface. In some cases, such as those shown in Fig. 10, the defect is almost tangential to the surface. This phenomenon can explain why high-fatigue-life polished specimens have the lowest fatigue strength of all unnotched specimen groups.

4. Discussion

From the results of the experiments there are some points which should be considered.

Regarding the behavior in the tensile tests, according to Fig. 2, it can be verified that there is very little difference among the specimens with different surface treatments, as expected, given that the treatments only affect a small part of the section of the specimen that is close to the surface. Hence, it can be concluded that the surface treatments used do

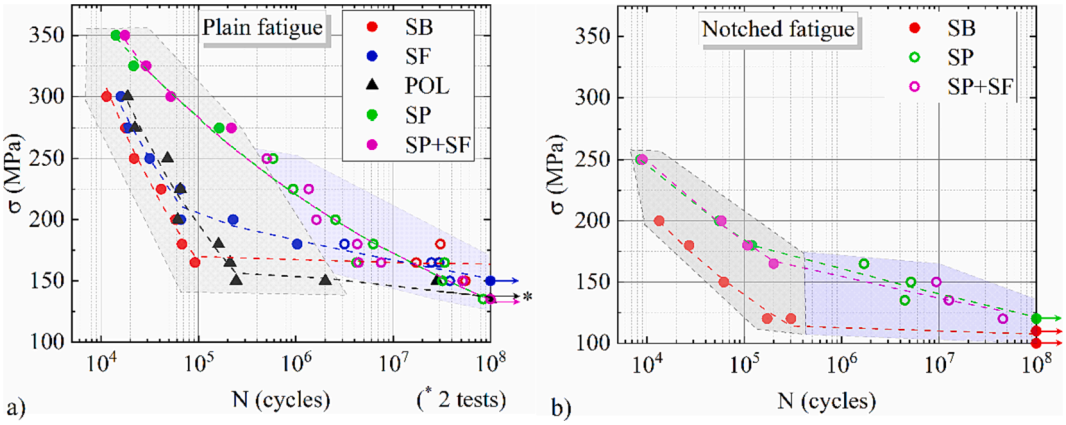

Fig. 7. Fatigue test results in smooth (7a) and notched (7b) specimens. Solid circular symbols, cracks initiated on the surface; hollow circular symbols, failures due to internal defects; triangular symbols, failures due to internal defects very close to the surface in polished specimens.

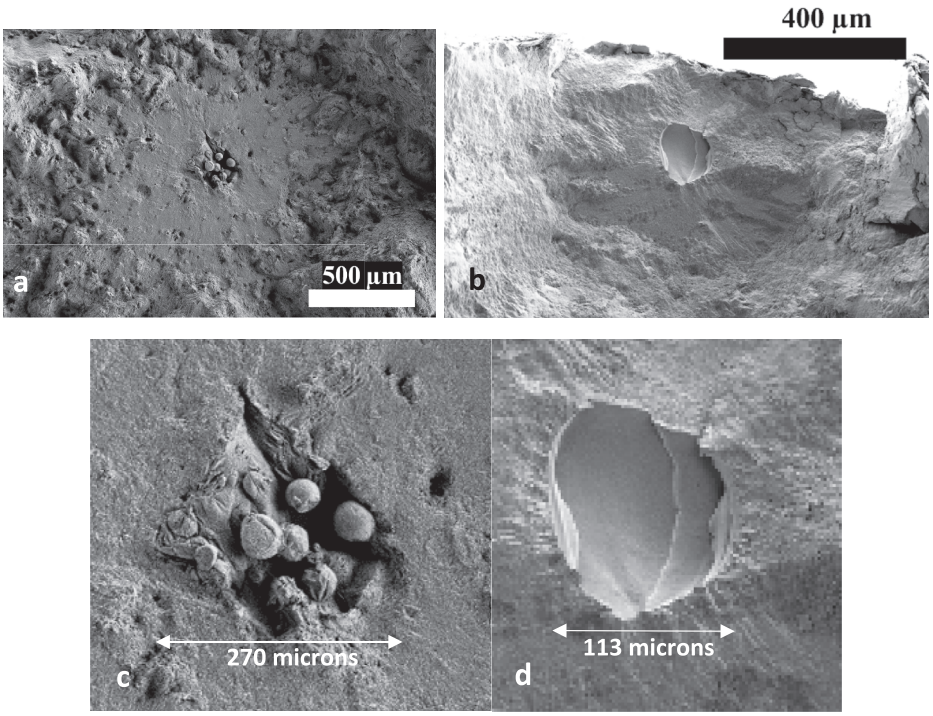

Fig. 8. Examples of type 1 fracture surfaces, corresponding to internal defect failures. (a) SP, 165 MPa, 3.9 10^6 cycles. (b) SP, 250 MPa, 5.9 10^5 cycles. (c) Starting defect in (a). (d) Starting defect in (b).

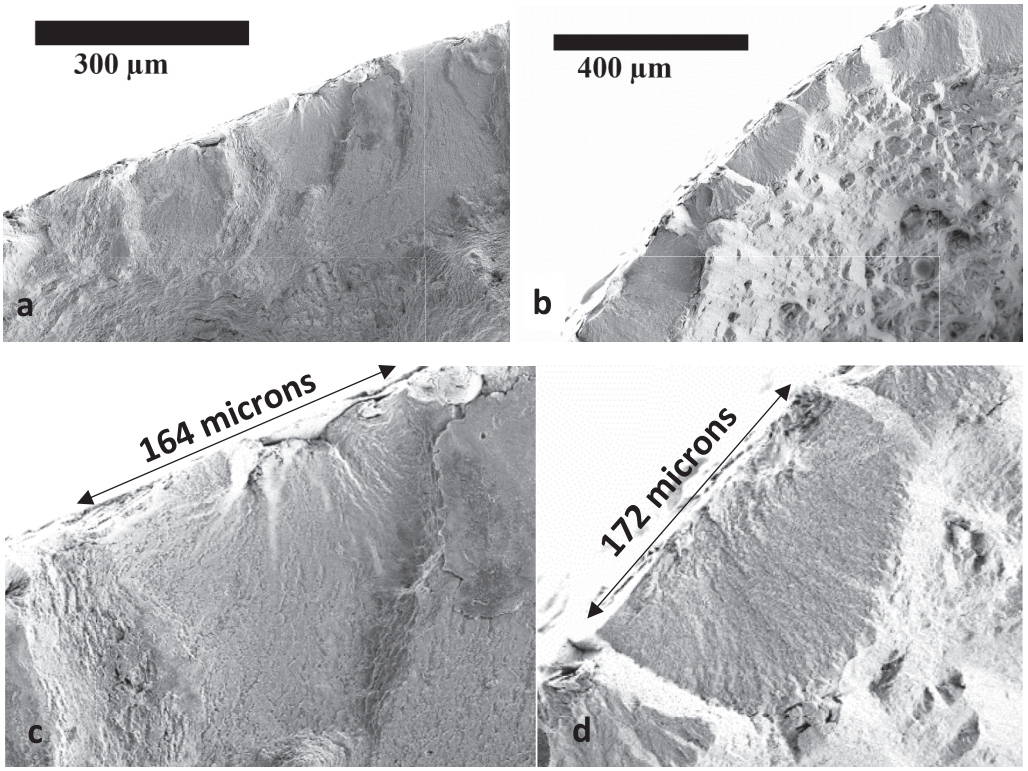

Fig. 9. Examples of type 2 fracture surfaces, corresponding to surface crack failure. (a) SPSF, 300 MPa, 5.2 10^6 cycles. (b) SP, 350 MPa, 14,500 cycles. (c) One of the cracks in (a). (d) One of the cracks in (b).

not significantly modify the static resistance of the samples. Conversely, the small strain hardening produced in this alloy and the high level of fracture deformation relative to other AlMg alloys can be appreciated [35,36]. This characteristic behavior can be explained to a large extent by the bimodal nature of the microstructure of the selective-laser-melted Scalmalloy elements [59,66].

Relative to fatigue behavior, it is worth noting the presence of different initiation points of the cracks that cause failure. For smooth

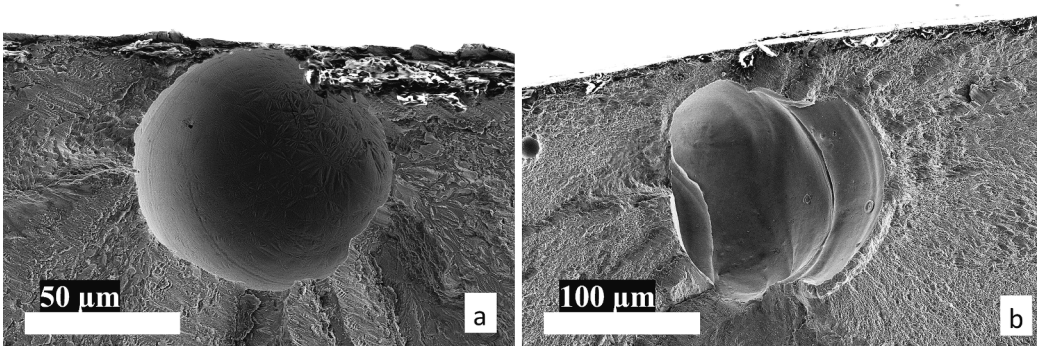

Fig. 10. Examples of fracture surfaces corresponding to failures initiated from an internal defect very close to the surface in polished specimens. (a) POL, 200 MPa, 6.1 10^4 cycles. (b) POL, 165 MPa, 2.2 10^5 cycles.

specimens, there are three different methods of initiating cracks. In polished specimens, all faults are initiated from defects very close to the surface. These defects approach the surface as a result of the 80-µm contour layer removed during polishing, moving the defects in the junction zone between the contour of the section and the inner zone to the surface. With the rest of the treatments, failures are initiated on the surface or inside the specimen. In general, for short lives, failures start on the surface, while for long lives, they start inside. Fig. 7a shows two different shaded areas distinguishing the types of failure. For the SB and SF treatments, from 10^6 to 10^8 cycles, failures start inside the specimens (blue zone), while for relatively short lives, they do so from the surface (gray zone). For SP and SPSF treatments, failures initiate from internal defects at higher stress levels than for SB treatment and with shorter lives, from $4x10^5$ to 10^8 cycles. For notched specimens, the change from surface initiation to internal initiation occurs for all treatments at lifetimes between $3x10^5$ and 10^6 cycles, as shown in Fig. 7b.

Another characteristic of the fatigue curves, especially for unnotched specimens, is that for intermediate lives of 10^5 to 10^6 cycles, the fatigue strengths of the SP and SPSF specimens are high, for 10^7 cycles, the strengths for all treatments are almost the same, and for lives above 10^7 cycles, the strengths of the SB and SF specimens are slightly higher than those of the SP and SPSF specimens. A possible explanation for this trend is that while initiation occurs on the surface, the high residual compressive stresses produced by the SP increase the small crack growth resistance of the shot-peened specimens. By decreasing the cyclic stress level, the residual compressive stresses close to the surface in the SP and SPSF specimens stop the small cracks emanating from the surface. However, the cracks initiated inside the specimens and outside the compressive residual stress field may continue growing. This stop in the surface cracks does not occur in the SB and SF specimens, which have low compressive residual stresses. For low stresses, surface cracks stop in the SB and SF specimens due to the presence of compressive residual stresses close to the surface, as shown in Fig. 6. Then, failures are initiated inside the specimens. For those stresses, initiation occurs in areas without compressive residual stresses with any type of specimen treatment. Moreover, for the SP and SPSF specimens, the residual stresses inside have higher tensile stresses than the SB and SF specimens to compensate for the higher compressive stresses on the surface. This phenomenon causes crack initiation to start earlier; however, as the initial crack grows toward the surface, in the SP and SPSF specimens, growth is delayed, counteracting the effect of the short duration of the crack initiation by starting in an area of significant residual tensile stresses. A possible explanation for the convergence of fatigue curves in the high-life zone is as follows. For lifetimes between 10^6 and 10^7 cycles, the delay produced by residual surface stresses in the SP and SPSF specimens compensates for the earlier crack initiation produced by tensile residual stresses, resulting in a similar life at the same stress levels. However, for lifetimes greater than 10^7 cycles, where the duration of the initiation and growth phase of small cracks is considerably longer than that of long crack propagation, the delays in growth toward the surfaces of the SP and SPSF specimens do not compensate for the earlier initiation phase produced by the tensile residual stresses; therefore, the total life becomes shorter in the SP and SPSF specimens than in the SB and SF specimens.

Regarding the notched specimen tests, the SN curve for the SB specimens shows a clear fatigue limit, and all failures are initiated on the surface. For nominal stresses below 120 MPa, stresses close to the surface are insufficient to initiate a crack or to make it grow after initiation. Conversely, stresses in the interior, which are close to the nominal stress, are insufficient to initiate an internal crack. Thus, a fatigue limit is produced. In contrast, for the SP and SPSF specimens, failures are initiated on the surface and from internal defects. The compressive residual stresses produced by SP stop cracks from initiating on the surface at a high nominal stress level ($\approx$ 170 MPa). Below this stress, cracks initiate from the interior, where there are small positive residual stresses, producing fatigue lives between 10^6 and 10^8 cycles. For lives near 10^8 cycles, the nominal strength in the net section of the specimens is close to the fatigue limit obtained for SB specimens. Again, the curves for the SP and SPSF specimens become closer to that for SB as the number of cycles increases, although they do not merge or cross, at least for lives lower than 10^8 cycles.

To understand the fatigue behavior of this material, a preliminary analysis based on fracture mechanics was carried out to follow cracks emanating from the surface. The objective was to associate the value of the global stress amplitude below which surface cracks do not initiate or stop growing just after initiation to a fatigue crack growth threshold of this material. A thorough analysis of the fracture surfaces and the defects producing the critical cracks has been planned for the near future. This analysis will allow a precise and detailed study of crack evolution considering surface and internal cracks and their growth. This study will consider the compressive residual stress fields produced by the surface treatments and the high stress gradient produced by the notch for notched components.

Initially, only a semicircular surface crack emanating from the surface of the notched or unnotched specimens was considered, and the evolution of ΔK while growing under different nominal stress amplitudes was analyzed. The stress gradient and stress fields produced by notches and surface treatments, respectively, have been included in the analysis. In all cases, the ΔK distribution was obtained with NASGRO 6.0 Software and using the SC02 crack geometry (semielliptical surface crack in plate – univariant WF) [67]. Using the SC02 crack geometry, and due to its weight function formulation (WF), it is possible to incorporate the effect of stress gradients in the calculation of ΔK, as is the case for residual stresses and notched geometries. Considering that only small cracks are going to be considered in this analysis, the ΔK values for each load and crack length have been obtained by assuming a semi-infinite space under the same stress field as that produced in the specimen. Therefore, instead of the real geometry of the specimen

shown on the left of Fig. 11 (solid cylinder), the specimens shown on the right of Fig. 11 (semi-infinite space) have been used for the analysis. Note that the geometry on the right is far from the cylindrical geometry, but the approximation is very precise, assuming that the crack length, a, is much smaller than the specimen radius, R.

Fig. 12a shows the fatigue results for unnotched specimens and two bands separating points representing failures initiated from the surface from those initiated from internal defects. The red band, ranging from 160 to 170 MPa, separates the results of the specimens with SB and SF treatments; the green band, ranging from 255 to 270 MPa, separates the results of the SP and SPSF specimens. Fig. 12b shows the evolution of ΔK for a small surface crack growing across the residual stress field produced by SB under different stress amplitudes. Note that the values of ΔK represented are the positive part of ΔK during the loading cycle with $R = -1$. Fig. 12c shows the ΔK evolution in the case of the residual stress field produced by SP under different stress amplitudes. In the case of Fig. 12b, assuming initial cracks smaller than 100 μm and taking into account the limits of the red band in Fig. 12a mentioned before, it seems logical to suppose that the stress intensity threshold, ΔK_{th}, is between 0.6 and 0.9 MPa$\sqrt{m}$; this threshold is represented by gray band in Fig. 12b, and it is a range given by some authors [49,50,56]. Considering the low stress in the red band of Fig. 12a and the highest ΔK_{th} in the gray band, Fig. 12b shows that for stresses lower than 160 MPa, a superficial crack must be longer than 120 μm to grow and break the specimen. No such type of superficial defect is found in the specimens that broke from an internal defect. For shot-peened specimens, Fig. 12c shows that under constant amplitude loading, ΔK decreases while the crack grows due to the compressive residual stress field produced by SP. By assuming the same ΔK_{th} value as before and a stress amplitude of 255 MPa, corresponding to the lowest stress value of the green band of Fig. 12a, this graph shows that a superficial crack must be longer than 190 μm to grow and break the specimen. No such type of superficial defect can be found in the specimens that break from an internal defect. Large initial defects, such as those shown in Figs. 8 and 10, require relatively high thresholds to stop under the same loads. For instance, 150-μm initial surface defects in sand-blasted specimens and 225-μm initial surface defects in shot-peened specimens require threshold values close to 1.5 MPa$\sqrt{m}$ to stop. These threshold values are in the range estimated by different authors for this alloy [59–62,68–70]: 0.65 [60] to 1.96 MPa$\sqrt{m}$ [59]. A precise estimation of the ΔK_{th} value that stops the growth of surface cracks can be obtained once the fracture surface and the initial small defects producing the failure are analyzed. Fig. 12a shows that for the SF specimens, the stress level at which surface and internal crack initiation is produced is slightly increased. This finding suggests that the initial defects in these specimens are slightly smaller than those in SB specimens. This phenomenon may occur because the finish eliminates a very small surface layer, reducing the defect size; however, it might be a statistical effect because relatively few specimens are tested at these stresses.

Fig. 12d shows the ΔK values of the polished samples, which do not have the compressive residual stresses of the SB and SP groups, and the specimens that have the lowest stresses in the tests. In this case, there is no plateau, as in SB, or a decrease, as in SP, in ΔK; therefore, it is easy to observe the growth of a small surface initial crack or defect and the breakage of a specimen. Fig. 12d shows the band of the possible threshold, ΔK_{th}, and it shows that even a 40-μm-long surface defect grows. As shown in Fig. 10, larger superficial defects are found in this group of tests, which is why in this group, there is not a transition for the type of failure; all the failures are initiated from the surface.

Following the same procedure for notched specimens, Fig. 13a shows the fatigue results for the notched specimens and the two bands separating points that represent failures initiated on the surfaces from those initiated from internal defects. The red band of SB specimens ranges from 100 to 105 MPa, and the green band ranges from 165 to 170 MPa. Fig. 13b shows the evolution of ΔK for a small surface crack growing across the residual stress field produced by SB under different stress amplitudes, and Fig. 13c shows the ΔK evolution in the case of the residual stress field produced by SP under different stress amplitudes. Again, under constant amplitude loading, ΔK decreases while the crack grows due to the compressive residual stress field produced by SP. Assuming the same threshold as in the unnotched specimens, $\Delta K_{th} = 0.9$ MPa$\sqrt{m}$. Fig. 13b shows that for a stress amplitude of 100 MPa in a specimen with SB, a superficial crack must be longer than 125 μm to grow and break the specimen, which is approximately the same value as that in the unnotched specimens. Fig. 13c shows that for a stress amplitude of 170 MPa in a specimen with SP, a superficial crack must be longer than 190 μm to grow and break the specimen, which is the same value as that in the unnotched specimens. Fig. 13b and 13c show that if $\Delta K_{th} = 1.5$ MPa$\sqrt{m}$, as assumed before for unnotched specimens, the crack lengths producing the change from the crack growing to not growing are 160 μm for the SB specimens and approximately 240 μm for the SP specimens. However, no such type of superficial defect can be found in the specimens that break from an internal defect.

According to the previous analysis, by considering the sizes of the first initial defects seen on the fracture surfaces, it can be said that there is a crack growth threshold for cracks emanating from the surface, which should be approximately between 0.6 and 1.5 MPa $\sqrt{m}$. Considering that tests have been carried out with a stress ratio of $R = -1$, that only the positive part of ΔK is considered, and that the cracks are small, this value is between the effective threshold $\Delta K_{th,eff}$ for short cracks, where plasticity- and roughness-induced closure have not been developed; the value seems to be near 0.6–0.9 MPa $\sqrt{m}$ [61,62,69], and the long crack threshold value is near 1.5–1.96 MPa $\sqrt{m}$ [59,61,62,68].

All this analysis and dissertation has dealt with cracks emanating from the surface. It has been assumed that if the crack does not start from

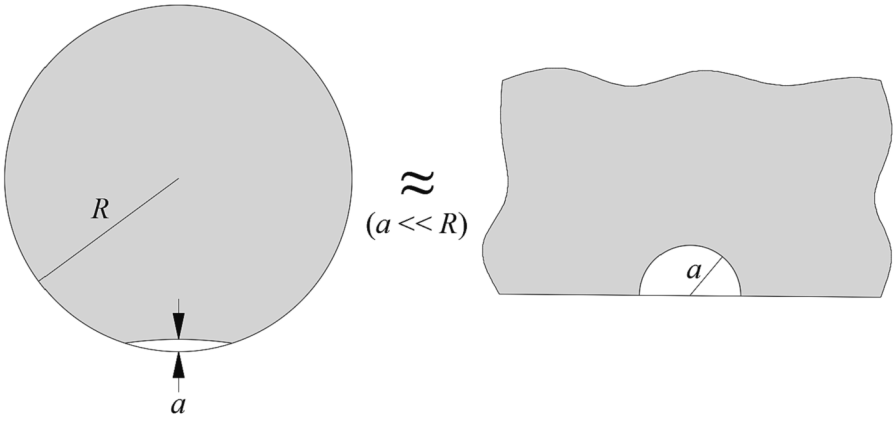

Fig. 11. Surface crack in a solid cylinder (left) and surface crack in a semi-infinite space (right).

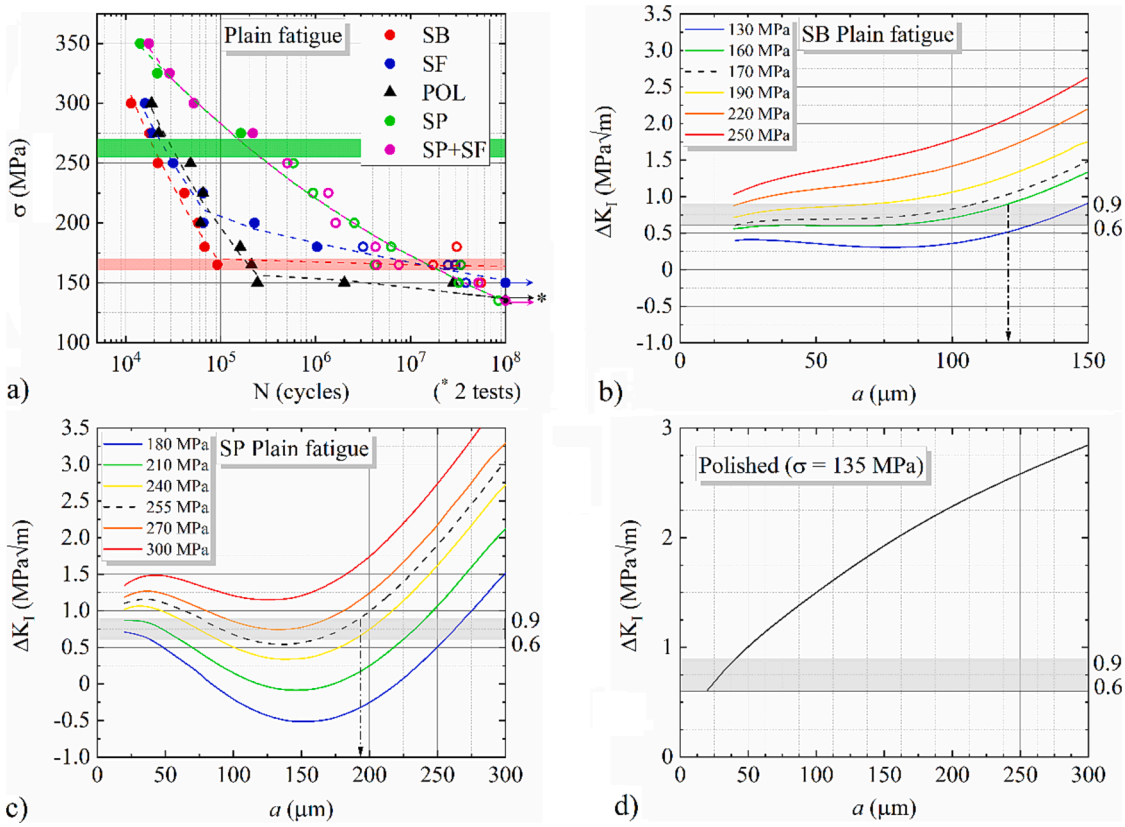

Fig. 12. A) s-N curves for unnotched specimens and stress bands where critical cracks change from surface to internal cracks; b) ΔK evolution of cracks growing from the surface with different stress amplitudes for unnotched sand-blasted specimens; c) ΔK unnotched shot-peened specimens; and d) ΔK in a polished specimen.

the surface it will start from an internal defect. But this is only an assumption, another detailed analysis will be needed in the future to study the cracks starting from internal defects. In this case it will be important to analyze the size and depth of the defect when comparing the stress intensity factor with the crack growth threshold. In this case there is an important issue, the crack in this situation is growing as if it was in vacuum where crack growth rate and threshold are different. These parameters are difficult to measure in this situation but they are necessary to do a rigorous comparison.

5. Conclusions

From the previous analysis, by comparing the effects of different surface treatments on the fatigue behaviors of notched and unnotched Scalmalloy additive manufactured specimens, some conclusions could be obtained.

-The polishing treatment had three main effects on the specimens: The surface finish was substantially improved, it eliminated compressive residual stresses that resulted from the sand blasting pretreatment and brought internal defects toward the surface. A combination of these three effects resulted in an overall decrease in the fatigue strength of the material relative to SB or SP. In addition, internal defects close to the surface and the lack of compressive residual stresses close to the surface caused all failures to initiate from defects very close to the surface.

-The treatment of shot peening had a main effect on the appearance of important residual compressive stresses near the surfaces of the samples, superior to those generated by the previous treatment of sand blasting. The surface roughness (R_a and R_z) was not significantly affected. Due to these residual stresses, an increase in the fatigue strength of the material was observed in most cases. When the failure was caused by an internal defect, that is, for lives longer than 10^6 cycles, the effects of these residual stresses on the fatigue life were relatively low. This effect decreased as the stress levels decreased and the fatigue lives increased. In specimens without notches, the fatigue curves of SB and SF tended to converge with the SP and SPSF curves in the zone with many cycles, where the internal failure mode was predominant for SF, SB, SP and SPSF. For notched specimens, the effect was similar, but the fatigue curves did not converge totally for lives under 10^8 cycles. Tests with lives above 10^6 cycles would give additional insight into this tendency.

-The isotropic finishing treatment or superfinishing improved the surface finish. Concerning fatigue, the effect of this treatment was very limited. A detailed microstructural analysis that searches for possible defects not eliminated by the treatment would allow a better understanding of the lack of fatigue strength improvement produced by the SF treatment.

-In the groups of specimens whose S-N curve presented two zones with differentiated slopes, the transition between failure types 1 and 2 (surface and internal) could be related to the change in slope. This relationship did not apply to polished specimens, which responded to failure mode 3 (defect very close to the surface).

-The change between surface and internal fatigue crack initiation seemed to be associated with a fatigue crack growth threshold for small surface cracks. This effect should be analyzed for internal cracks considering the residual stresses in the initiation zone, the initial defect size, the evolution of the crack growing across the residual stress field and the different crack growth properties when the crack grew without contact with the atmosphere. This study would give us further insight into a possible threshold for these internal cracks in the same manner as can be found in the literature [19,47], but considering lives reaching 10^8 cycles.

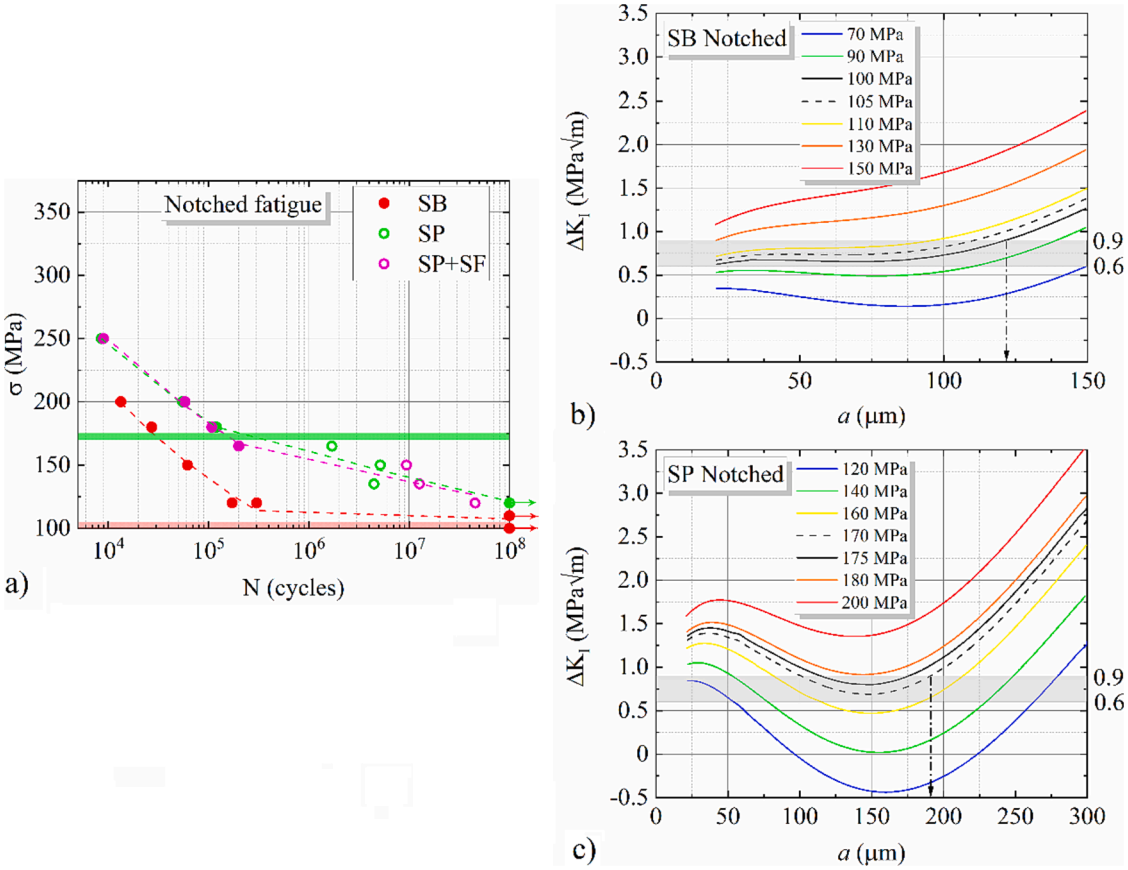

Fig. 13. A) S-N curves for notched specimens and stress bands where critical cracks change from surface to internal cracks; b) ΔK evolution of cracks growing from the surface with different stress amplitudes for notched sand-blasted specimens; and c) ΔK in notched shot-peened specimens.

CRediT authorship contribution statement

Santiago Aguado-Montero: Software, Investigation. **Jesús Vázquez:** Methodology, Writing – review & editing, Visualization. **Carlos Navarro:** Methodology, Writing – review & editing, Funding acquisition. **Jaime Domínguez:** Conceptualization, Methodology, Writing – original draft.

Declaration of competing interest

The authors declare that they have no known competing financial interests or personal relationships that could have appeared to influence the work reported in this paper.

Data availability

Data will be made available on request.

Acknowledgements

The authors thank the Junta de Andalucía and the European Fund for Regional Development for their financial support through the investigation project PY20-FR-01079.

References

[1] Meyer J, Barnes JE. Scalmalloy® is too expensive and design optimisation only makes sense in aerospace. True or false? Metal Additive Manufacturing, 2019, 5, 127–135. https://issuu.com/inovar-communications/docs/mam_spring_2019_sp/127?fr=sMmZkNTExNTgwNDU.

[2] Zhang X, Liang E. Metal additive manufacturing in aircraft: current application, opportunities and challenges. In: IOP Conference Series: Materials Science and Engineering, Vol. 493. IOP Publishing; 2019. p. 012032. https://doi.org/10.1088/1757-899X/493/1/012032.

[3] Plocher J, Panesar A. Review on design and structural optimisation in additive manufacturing: towards next-generation lightweight structures. Mater Des 2019; 183:108164. https://doi.org/10.1016/j.matdes.2019.108164.

[4] du Plessis A, Razavi SMJ, Benedetti M, Murchio S, Leary M, Watson M, et al. Properties and applications of additively manufactured metallic cellular materials: a review. Prog Mater Sci 2022;125:100918. https://doi.org/10.1016/j.pmatsci.2021.100918.

[5] Liu X, Zhao C, Zhou X, Shen Z, Liu W. Microstructure of selective laser melted AlSi10Mg alloy. Mater Des 2019;168:107677. https://doi.org/10.1016/j.matdes.2019.107677.

[6] Aboulkhair NT, Everitt NM, Ashcroft I, Tuck C. Reducing porosity in AlSi10Mg parts processed by selective laser melting. Addit Manuf 2014;1:77–86. https://doi.org/10.1016/j.addma.2014.08.001.

[7] Mfusi BJ, Mathe NR, Tshabalala LC, Popoola PA. The effect of stress relief on the mechanical and fatigue properties of additively manufactured AlSi10Mg parts. Metals 2019;9(11):1216. https://doi.org/10.3390/met9111216.

[8] Maleki E, Bagherifard S, Guagliano M. Application of artificial intelligence to optimize the process parameters effects on tensile properties of Ti-6Al-4V fabricated by laser powder-bed fusion. Int J Mech Mater Des 2022;18:199–222. https://doi.org/10.1007/s10999-021-09570-w.

[9] Pegues JW, Shao S, Shamsaei N, Sanaei N, Fatemi A, Warner DH, et al. Fatigue of additive manufactured Ti-6Al-4V, Part I: the effects of powder feedstock, manufacturing, and post-process conditions on the resulting microstructure and defects. Int J Fatigue 2020;132:105358. https://doi.org/10.1016/j.ijfatigue.2019.105358.

[10] Morettini G, Razavi SMJ, Zucca G. Effects of build orientation on fatigue behavior of Ti-6Al-4V as-built specimens produced by direct metal laser sintering. Procedia Struct Integr 2019;24:349–59. https://doi.org/10.1016/j.prostr.2020.02.032.

[11] Slawik S, Bernarding S, Lasagni F, Navarro C, Periñán A, Boby F, et al. Microstructural analysis of selective laser melted Ti6Al4V modified by laser peening and shot peening for enhanced fatigue characteristics. Mater Charact 2021;173:110935. https://doi.org/10.1016/j.matchar.2021.110935.

[12] Aguado-Montero S, Navarro C, Vázquez J, Lasagni F, Slawik S, Domínguez J. Fatigue behaviour of PBF additive manufactured TI6AL4V alloy after shot and laser peening. Int J Fatigue 2022;154:106536. https://doi.org/10.1016/j.ijfatigue.2021.106536.

[13] Zhang J, Song B, Wei Q, Bourell D, Shi Y. A review of selective laser melting of aluminum alloys: processing, microstructure, property and developing trends.

J Mater Sci Technol 2019;35:270–84. https://doi.org/10.1016/j.jmst.2018.09.004.
[14] Louvis E, Fox P, Sutcliffe CJ. Selective laser melting of aluminum components. J Mater Process Technol 2011;211:275–84. https://doi.org/10.1016/j.matprotec.2010.09.019.
[15] Aboulkhair NT, Simonelli M, Parry L, Ashcroft I, Tuck C, Hague R. 3D printing of aluminium alloys: additive manufacturing of aluminium alloys using selective laser melting. Prog Mater Sci December 2019;106:100578. https://doi.org/10.1016/j.pmatsci.2019.100578.
[16] Damon J, Dietrich S, Vollert F, Gibmeier J, Schulze V. Process dependent porosity and the influence of shot peening on porosity morphology regarding selective laser melted AlSi10Mg parts. Addit Manuf 2018;20:77–89. https://doi.org/10.1016/j.addma.2018.01.001.
[17] Aboulkhair NT, Maskery I, Tuck C, Ashcroft I, Everitt NM. Improving the fatigue behaviour of a selectively laser melted aluminium alloy: Influence of heat treatment and surface quality. Mater. Des. 2016;104:174–82. https://doi.org/10.1016/j.matdes.2016.05.041.
[18] Buchbinder D, Schleifenbaum H, Heidrich S, Meiners W, Bültmann JJPP. High power selective laser melting (HP SLM) of aluminum parts. Physics Procedia 2011;12:271–8. https://doi.org/10.1016/j.phpro.2011.03.035.
[19] Brandl E, Heckenberger U, Holzinger V, Buchbinder D. Additive manufactured AlSi10Mg samples using Selective Laser Melting (SLM): Microstructure, high cycle fatigue, and fracture behavior. Mater Des 2012;34:159–69. https://doi.org/10.1016/j.matdes.2011.07.067.
[20] Sistiaga MLM, Mertens R, Vrancken B, Wang X, Van Hooreweder B, Kruth J, et al. Changing the alloy composition of A17075 for better processability by selective laser melting. J Mater Process Technol 2016;238:437–45. https://doi.org/10.1016/j.jmatprotec.2016.08.003.
[21] Qi T, Zhu H, Zhang H, Yin J, Ke L, Zeng X. Selective laser melting of Al7050 powder: melting mode transition and comparison of the characteristics between the keyhole and conduction mode. Mater Des 2017;135:257–66. https://doi.org/10.1016/j.matdes.2017.09.014.
[22] Martin JH, Yahata BD, Hundley JM, Mayer JA, Schaedler TA, Pollock TM. 3D printing of high-strength aluminium alloys. Nature 2017;549:365. https://doi.org/10.1038/nature23894.
[23] Stopyra W, Gruber K, Smolina I, Kurzynowski T, Kuźnicka B. Laser powder bed fusion of AA7075 alloy: influence of process parameters on porosity and hot cracking. Addit Manuf October 2020;35:101270. https://doi.org/10.1016/j.addma.2020.101270.
[24] Mair P, Goettgens VS, Rainer T, Weinberger N, Letofsky-Papst I, Mitsche S, et al. Laser powder bed fusion of nano-CaB6 decorated 2024 aluminum alloy. J Alloy Compd 2021;863:158714. https://doi.org/10.1016/j.jallcom.2021.158714.
[25] Abe F, Osakada K, Shiomi M, Uematsu K, Matsumoto M. The manufacturing of hard tools from metallic powders by selective laser melting. J Mater Process Technol 2001;111(1–3):210–3. https://doi.org/10.1016/S0924-0136(01)00522-2.
[26] Dadbakhsh S, Mertens R, Vanmeensel K, Vleugels J, Humbeeck JV, Kruth J-P. In situ alloying and reinforcing of Al6061 during selective laser melting. Proc CIRP 2018;74:39–43. https://doi.org/10.1016/j.procir.2018.08.009.
[27] Kaufmann N, Imran M, Wischeropp TM, Emmelmann C, Siddique S, Walther F. Influence of process parameters on the quality of aluminium alloy en AW 7075 using Selective Laser Melting (SLM). Phys Procedia 2016;83:918–26. https://doi.org/10.1016/j.phpro.2016.08.096.
[28] Mertens R, Dadbakhsh S, Van Humbeeck J, Kruth JP. Application of base plate preheating during selective laser melting. Procedia CIRP 2018;74:5–11. https://doi.org/10.1016/j.procir.2018.08.002.
[29] Tan Q, Zhang J, Sun Q, Fan Z, Li G, Yin Y, et al. aluminium alloy with titanium nanoparticles. Acta Mater 2024;196(2020):1–16. https://doi.org/10.1016/j.actamat.2020.06.026.
[30] Huang H, Jiang F, Zhou J, Wei L, Qu J, Liu L. Effects of Al-3(Sc, Zr) and shear band formation on the tensile properties and fracture behavior of Al-Mg-Sc-Zr alloy. J Mater Eng Perform 2015;24:4244–52. https://doi.org/10.1007/s11665-015-1748-y.
[31] Røyset J, Ryum N. Scandium in aluminium alloys. Int Mater Rev 2013;50(1):19–44. https://doi.org/10.1179/174328005X14311.
[32] Filatov YA, Yelagin VI, Zakharov VV, Alloys N-M-S. Mater Sci Eng, A 2000;280(1):97–101. https://doi.org/10.1016/S0921-5093(99)00673-5.
[33] Chen Q, Pan Q, Wang Y. Microstructure and mechanical properties of Al-5.8Mg-Mn-Sc-Zr alloy after annealing treatment. J Cent South Univ 2012;19(7):1785–90. https://doi.org/10.1007/s11771-012-1208-x.
[34] Kendig KL, Miracle DB. Strengthening mechanisms of an Al-Mg-Sc-Zr alloy. Acta Mater 2002;50:4165–75. https://doi.org/10.1016/S1359-6454(02)00258-6.
[35] Muhammad M, Nezhadfar PD, Thompson S, Saharan A, Phan N, Shamsaei N. A comparative investigation on the microstructure and mechanical properties of additively manufactured aluminum alloys. Int J Fatigue 2021;146:106165. https://doi.org/10.1016/j.ijfatigue.2021.106165.
[36] Nezhadfar PD, Thompson S, Saharan A, Phan N, Shamsaei N. Structural integrity of additively manufactured aluminum alloys: Effects of build orientation on microstructure, porosity, and fatigue behavior. Addit. Manuf. 2021;47:102292. https://doi.org/10.1016/j.addma.2021.102292.
[37] Li R, Wang M, Yuan T, Song B, Chen C, Zhou K, et al. Selective laser melting of a novel Sc and Zr modified Al-6.2 Mg alloy: processing, microstructure, and properties. Powder Technol 2017;319:117–28. https://doi.org/10.1016/j.powtec.2017.06.050.
[38] Zhou L, Pan H, Hyer H, Park S, Bai Y, McWilliams B, et al. Microstructure and tensile property of a novel AlZnMgScZr alloy additively manufactured by gas atomization and laser powder bed fusion. Scr Mater 2019;158:24–8. https://doi.org/10.1016/j.scriptamat.2018.08.025.
[39] Li R, Chen H, Chen C, Zhu H, Wang M, Yuan T, et al. Selective laser melting of gas atomized Al–3.02Mg–0.2Sc–0.1Zr alloy powder: microstructure and mechanical properties. Adv Eng Mater 2019;21:1800650. https://doi.org/10.1002/adem.201800650.
[40] APWORKS GmbH, https://www.apworks.de/scalmalloy.
[41] Spierings AB, Dawson K, Heeling T, Uggowitzer PJ, Schäublin R, Palm F, et al. Microstructural features of Sc- and Zr-modified Al-Mg alloys processed by selective laser melting. Mater Des 2017;115:52–63. https://doi.org/10.1016/j.matdes.2016.11.040.
[42] Jägle EA, Sheng Z, Wu L, Lu L, Risse J, Weisheit A, Raabe D. Precipitation reactions in age-hardenable alloys during laser additive manufacturing. Jom 2016;68:943–9. https://doi.org/10.1007/s11837-015-1764-2.
[43] Spierings AB, Dawson K, Kern K, Palm F, Wegener K. SLM-processed Sc-and Zr-modified Al-Mg alloy: mechanical properties and microstructural effects of heat treatment. Mater Sci Eng A 2017;701:264–73. https://doi.org/10.1016/j.msea.2017.06.089.
[44] Spierings AB, Dawson K, Voegtlin M, Palm F, Uggowitzer PJ. Microstructure and mechanical properties of as-processed scandium modified aluminium using selective laser melting. CIRP Ann Manuf Technol 2016;65:213–6. https://doi.org/10.1016/j.cirp.2016.04.057.
[45] Aboulkhair NT, Maskery I, Tuck C, Ashcroft I, Everitt NM. Improving the fatigue behaviour of a selectively laser melted aluminium alloy: Influence of heat treatment and surface quality. Mater Des 2016;104:174–82. https://doi.org/10.1016/j.matdes.2016.05.041.
[46] Leon A, Aghion E. Effect of surface roughness on corrosion fatigue performance of AlSi10Mg alloy produced by Selective Laser Melting (SLM). Mater Charact 2017;131:188–94. https://doi.org/10.1016/j.matchar.2017.06.029.
[47] Hamidi Nasab M, Giussani A, Gastaldi D, Tirelli V, Vedani M. Effect of surface and subsurface defects on fatigue behavior of AlSi10Mg alloy processed by laser powder bed fusion (L-PBF). Metals 2019;9(10):1063. https://doi.org/10.3390/met9101063.
[48] Bagherifard S, Beretta N, Monti S, Riccio M, Bandini M, Guagliano M. On the fatigue strength enhancement of additive manufactured AlSi10Mg parts by mechanical and thermal post-processing. Mater Des 2018;145:28–41. https://doi.org/10.1016/j.matdes.2018.02.055.
[49] Brandão AD, Gumpinger J, Gschweitl M, Seyfert C, Hofbauer P, Ghidini T. Fatigue properties of additively manufactured AlSi10Mg—surface treatment effect. Procedia Struct Integr 2017;7:58–66. https://doi.org/10.1016/j.prostr.2017.11.061.
[50] Uzan NE, Ramati S, Shneck R, Frage N, Yeheskel O. On the effect of shot-peening on fatigue resistance of AlSi10Mg specimens fabricated by additive manufacturing using selective laser melting (AM-SLM). Addit Manuf 2018;21:458–64. https://doi.org/10.1016/j.addma.2018.03.030.
[51] Maleki E, Bagherifard S, Unal O, Bandini M, Guagliano M. On the effects of laser shock peening on fatigue behavior of V-notched AlSi10Mg manufactured by laser powder bed fusion. Int J Fatigue 2022;163:107035. https://doi.org/10.1016/j.ijfatigue.2022.107035.
[52] du Plessis A, Glaser D, Moller H, Mathe N, Tshabalala L, Mfusi B, et al. Pore closure effect of laser shock peening of additively manufactured AlSi10Mg, 3D. Printing Addit Manufact 2019;6(5):245–52. https://doi.org/10.1089/3dp.2019.0064.
[53] Biddlecom JL. The Effects of Laser Shock Peening on the Fatigue Life of Additive Manufactured AlSi10Mg; 2023. PhD Dissertation, Clemson University. https://tigerprints.clemson.edu/all_dissertations/3328.
[54] Begoc S, Montredon F, Pommatau G, Leger G, Gas M, Eyrignoux S. Additive manufacturing of Scalmalloy® satellite parts, 8th European Conference for Aeronautics and Space Sciences (Eucass), 2019. https://doi.org/10.13009/EUCASS2019-677.
[55] Martucci A, Aversa A, Manfredi D, Bondioli F, Biamino S, Ugues D, et al. Low-power laser powder bed fusion processing of Scalmalloy®. Materials 2022;15:3123. https://doi.org/10.3390/ma15093123.
[56] Musekamp J, Reiber T, Hoche HC, Oechsner M, Weigold M, Abele E. Influence of LPBF-surface characteristics on fatigue properties of Scalmalloy®. Metals 1961;2021:11. https://doi.org/10.3390/met11121961.
[57] Raab M, Bambach M. Fatigue properties of Scalmalloy® processed by laser powder bed fusion in as-built, chemically and conventionally machined surface condition. J Mater Process Tech 2023;311:117811. https://doi.org/10.1016/j.jmatprotec.2022.117811.
[58] Schimbäck D, Mair P, Kaserer L, Perfler L, Palm F, Leichtfried G, et al. An improved process scan strategy to obtain high-performance fatigue properties for Scalmalloy®. Mater Des 2022;224:111410. https://doi.org/10.1016/j.matdes.2022.111410.
[59] Schimbäck D, Kaserer L, Mair P, Palm F, Leichtfried G, Pogatscher S, et al. Deformation and fatigue behaviour of additively manufactured Scalmalloy® with bimodal microstructure. Int J Fatigue 2023;172:107592. https://doi.org/10.1016/j.ijfatigue.2023.107592.
[60] Qin Z, Kang N, Zong H, Zhan C, Fang Y, Wang Z, et al. Huang Improved fatigue properties of laser powder bed fusion of Al–4.74Mg–0.70Sc–0.32Zr alloy via hot isostatic pressing. Mater Res Lett 2022;10(11):720–7. https://doi.org/10.1080/21663831.2022.2088252.
[61] Chernyshova P, Guraya T, Singamneni S, Zhu T, Chen ZW. Fatigue crack growth behavior of Al-4.5Mg-0.6Sc-0.3Zr alloy processed by laser powder bed fusion. J Mater Eng Perform 2021;30:6743–51. https://doi.org/10.1007/s11665-021-05989-6.

[62] Jonesa R, Cizek J, Kovarik O, Lang J, Ang A, Michopoulos JG. Describing crack growth in additively manufactured Scalmalloy. Additive Manufact Lett 2021;1:100020. https://doi.org/10.1016/j.addlet.2021.100020.
[63] Jones R, Cizek J, Kovarik O, Ang A, Champagne V. Observations on comparable aluminium alloy crack growth curves: Additively manufactured Scalmalloy®as an alternative to AA5754 and AA6061-T6 alloys? Additive Manufact Lett 2022;2:100026. https://doi.org/10.1016/j.addlet.2022.100026.
[64] Zavatta N, Troiani E. Preliminary tests on additive-manufactured Al-Sc specimens for the setup of a numerical model for Laser Shock Peening. J Phys Conf Ser 2023;2526:012044. https://doi.org/10.1088/1742-6596/2526/1/012044.
[65] Schajer GS. Application of finite element calculations to residual stress measurements; 1981. https://doi.org/10.1115/1.3224988.
[66] Zha M, Zhang HM, Yu ZY, Zhang XH, Meng XT, Wang HY, et al. Bimodal microstructure – a feasible strategy for high-strength and ductile metallic materials. J Mater Sci Technol 2018;34:257–64. https://doi.org/10.1016/j.jmst.2017.11.018.
[67] NASGRO Fracture Mechanics & Fatigue Crack Growth Software, SwRI, https://www.swri.org/consortia/nasgro.
[68] Hua Q, Li R, Wang M, Zhu H, Liu X, Lai D, et al. High cycle fatigue property of Al–Mg–Sc–Zr alloy fabricated by laser powder bed fusion. Adv Eng Mater 2023;25:2300352. https://doi.org/10.1002/adem.202300352.
[69] Qin Z, Kang N, El Mansori M, Wang Z, Wang H, Lin X, et al. Anisotropic high cycle fatigue property of Sc and Zr-modified Al-Mg alloy fabricated by laser powder bed fusión. Addit Manuf 2022;49:102514. https://doi.org/10.1016/j.addma.2021.102514.
[70] K. Schmidtke. Qualification of SLM Additive Manufacturing for Aluminium, PhD Dissertation, Technischen Universität Hamburg, 2020. https://doi.org/10.15480/882.2551.